Progress In Electromagnetics Research C, Vol. 172, 336–349, 2026

PIER C

(Received 2 June 2026, Accepted 21 July 2026, Scheduled 14 August 2026)

Compact Self-Decoupled Six-Port MIMO Antenna with High Isolation for 5G mmWave Applications

Malini Soman[1,*], Pardeep Kumar[2], Manish Sharma[3], Seema[1], and Kishore A. K. Ayyala[4]

[1]*Department of Electronics and Communication Engineering, Faculty of Engineering & Technology SGT University, Gurugram, Haryana 122505, India*
[2]*School of Computer Science and Engineering, IILM University, Greater Noida, UP, India*
[3]*SMIEEE, Department of Electrical, Electronics and Communication Engineering Galgotias University, Greater Noida, Uttar Pradesh 203201, India*
[4]*Department of Electronics and Communication Engineering, School of Engineering and Technology KR Mangalam University, Gurugram, Haryana 122103, India*

ABSTRACT: Compact multi-port antennas are essential for future 5G millimetre-wave systems because they support high-speed communication, stable signal quality, and multiple data channels within limited device space. This study presents a compact, planar, six-port MIMO antenna for 38–40 GHz 5G millimetre-wave applications. The antenna is designed on a low-loss Rogers RT5880 substrate with an overall size of $40 \times 40 \times 0.543\,\text{mm}^3$. The design follows an S-parameter-guided approach, beginning with a single radiating element and extending to the final six-port MIMO configuration. The proposed structure maintains a simple planar geometry without using decoupling networks, electromagnetic bandgap cells, frequency-selective surfaces, metasurfaces, dielectric lenses, or external reflectors. Simulated and measured results show good impedance matching across 38–40 GHz, with reflection coefficients below -10 dB and resonance near 39.3–39.5 GHz. Inter-port isolation is mostly better than 20 dB, while the measured gain reaches approximately 8.28 dBi near resonance. The antenna also achieves an acceptable low ECC of 5×10^{-4}, a diversity gain close to 10 dB, an acceptable TARC, and a balanced MEG. Such results validate its applicability to compact 5G user equipment, small-cell systems, and high-density wireless platforms.

1. INTRODUCTION

The rapid expansion of fifth-generation (5G) wireless communication networks necessitates radiating systems capable of delivering ultra-high data rates, near-zero latency, and robust spectral efficiency. To satisfy these stringent performance metrics, the millimeter-wave (mmWave) spectrum — particularly the 28–40 GHz frequency band — has emerged as a pivotal enabler due to its expansive unallocated bandwidth. However, mmWave propagation is intrinsically limited by severe free-space path loss, atmospheric absorption, and high susceptibility to signal blockages. Multiple-input multiple-output (MIMO) technology has proven indispensable in mitigating these channel degradation factors, effectively enhancing channel capacity, spatial diversity, and overall link reliability without demanding additional spectral resources [1, 2].

Consequently, contemporary literature has extensively investigated the scaling and optimization of compact MIMO configurations tailored for 5G ecosystems. Early research primarily focused on two-port architectures, employing configurations such as composite patches, coplanar waveguide (CPW) feeds with dual-polarization, dielectric lenses, and metamaterial-walled monopole radiators to achieve stable impedance matching and high-gain characteristics [3–6]. As the imperative for higher data throughput escalated, researchers systematically expanded these topologies into four-port architectures. A multitude of standard four-port designs operating across the 28/38 GHz bands have been documented, capitalizing on optically transparent substrates, Yagi-Uda elements, hexa-band patches, fractal geometries, reconfigurable structures, tri-circular rings, and miniaturized flexible layouts [7–21]. These topologies successfully managed inter-element coupling through rigorous geometric optimization and structural positioning.

To push the boundaries of isolation and gain enhancement in compact systems, advanced decoupling methodologies have been widely integrated into recent array designs. Implementations leveraging dedicated decoupling structures (DS), electromagnetic bandgap (EBG) components, metasurfaces, frequency-selective surfaces (FSS), and machine-learning-based gain predictions have demonstrated significant mutual coupling suppression [22–29]. Nevertheless, these isolation-enhancement techniques often introduce inherent trade-offs: they impose significant structural complexity, demand stringent fabrication tolerances, and substantially increase the overarching footprint of the antenna system.

To enhance spatial multiplexing in dense communication environments, higher-order MIMO systems have attracted significant research interest. Eight-port MIMO antennas with high isolation have been reported for dual-band 28/38 GHz and wideband mmWave applications [30, 31]. In addition, wideband arrays operating in the 37–40 GHz spectrum (n260/n262 bands) have employed characteristic mode analy-

* Corresponding author: Malini Soman (Malu7280@gmail.com).

TABLE 1. Summary of reported MIMO antennas operating near the 38–40 GHz band.

Ref.	Antenna type (Ports)	Substrate	Size (mm)	Gain (dBi)	Isolation (dB)	ECC
[3]	2-port composite patch	Rogers RO3003	$7.5 \times 8.8 \times 0.25$	5.86	< -20	0.002
[4]	2-port dual-band dual-polarized	Rogers RO4003	$3.77\lambda_0 \times 1.86\lambda_0$	> 8	> 20	< 0.0001
[5]	Dual-port with lens	Planar antenna + 3D lens	$19 \times 29 \times 13$	11.40	> 22	< 0.5
[7]	4-element optically transparent	AgHT-8/Plexiglas	$24 \times 20 \times 1.85$	> 3	> 16	< 0.1
[8]	4-port Yagi-Uda	Rogers RO3003	$21.6 \times 20 \times 0.25$	~ 9	< -35	≈ 0
[9]	E-shaped H-slotted 4-port	Rogers RT5880	$20 \times 24 \times 0.543$	7.90	28	0.0005
[10]	Four-element Hexa-band Patch	Rogers RT/Duroid 5880	$52 \times 52 \times 0.8$	10.73	> 25	$< 1 \times 10^{-6}$
[11]	4-port SRR-loaded planar	Rogers RT5880	$14 \times 14 \times 0.8$	6.02	> 25	< 0.005
[12]	4-port compact dual-band	Rogers-based	$26 \times 26 \times 0.25$	8.10	~ 33	0.0005
[13]	Quad-port 38 GHz	RT/Duroid 5880	$35 \times 30 \times 0.8$	10.24	> 20	< 0.0002
[14]	Quad-element SBFP	Rogers RT5880	$30 \times 30 \times 0.8$	10.07	> 17	$\leq 1 \times 10^{-4}$
[15]	Flexible 4-port wearable	Rogers RO3003	$18 \times 8.5 \times 0.25$	7.73	> 20	< 0.03
[16]	Reconfigurable 28/38 GHz	Rogers RT5880	$22.5 \times 30 \times 0.787$	6.50	-40	1.6×10^{-4}
[17]	4-port tri-circular ring	Flexible RO5880	$23 \times 18 \times 0.254$	6.60	> 18	0.0017
[18]	4-port 28/38 GHz wideband	Rogers RT/Duroid 5880	$5 \times 9.7 \times 2.25$	8.30	> 21	0.00007
[19]	Flexible triple-band 4-port	Rogers RO3003	$14.5 \times 48 \times 0.25$	8.48	> 20	< 0.046
[20]	Miniaturized dual-band 4-port	Low-loss substrate	$15 \times 15 \times 0.8$	8.64	> 25	< 0.001
[22]	Quad-port microstrip with DS	Rogers TMM4	$17.76 \times 17.76 \times 1.52$	8.70	< -35	$< 1.5 \times 10^{-4}$
[23]	4-port EBG	Rogers TMM4	$17.76 \times 17.76 \times 1.52$	8.90	-25 to -90	$< 3 \times 10^{-5}$
[24]	Quad-port mmWave with MS + FSS	Rogers RT5880	$28 \times 28 \times 0.508$	10.35	> 25	< 0.001
[25]	FSS-loaded quad-port	Rogers RO4003C	$25.7 \times 25.7 \times 0.238$	~ 8	≤ -22	≤ 0.002
[26]	ML-based 4-port 38 GHz	Rogers RT5880	$37 \times 24 \times 0.787$	8.09	27	< 0.02
[27]	ML-based 28/38 GHz 4-port	Rogers RT5880	$3.34\lambda_0 \times 3.34\lambda_0$	10.14	> 29	< 0.02
[28]	Four-element Self-Decoupled	Rogers RT5880	$19 \times 15 \times 1.575$	13.40	> 40	< 0.0009
[29]	Four-element Window-shaped	Rogers RO5880	$24 \times 32 \times 0.254$	6.20	> 20	< 0.005
[30]	Eight-element dual-band smartphone	FR4	$150 \times 70 \times 0.8$	≈ 5.40	> 10	≤ 0.15
[31]	8-port wideband	Rogers RT/Duroid 5880	$44 \times 70 \times 0.8$	8.50	30	0.00007
Proposed	**Six-port MIMO antenna**	**Rogers RT5880**	$\mathbf{40 \times 40 \times 0.543}$	**8.28 dB**	$\mathbf{> 20}$ **dB**	$\mathbf{< 0.001}$

sis (CMA), dual-key slot radiators, and metasurface reflectors to improve radiation performance and electromagnetic field confinement [32, 33].

As summarized in Table 1, substantial progress has been achieved in mmWave MIMO antenna design across different port configurations. However, compact six-port antennas remain relatively limited, and high isolation is frequently achieved via auxiliary decoupling techniques or increased structural complexity. These challenges motivate the development of a compact planar six-port MIMO antenna that inherently provides high isolation while maintaining a simple architecture.

The primary contributions of this work are summarized as follows:

1. Compact Six-Port MIMO Antenna: A compact planar six-port MIMO antenna operating in the 38–40 GHz band for 5G mmWave applications.
2. Low-Profile Implementation: Realization on a Rogers RT5880 substrate with overall dimensions of $40 \times 40 \times 0.543\,\text{mm}^3$.
3. Self-Decoupled Operation: Inter-element isolation exceeding 20 dB achieved through an optimized radiator topology and symmetric element arrangement, without employing DGS, EBG structures, FSS, metasurfaces, lenses, neutralization lines, or external decoupling networks.
4. Comprehensive Performance Validation: Simulated and measured characterization, including gain, envelope cor-

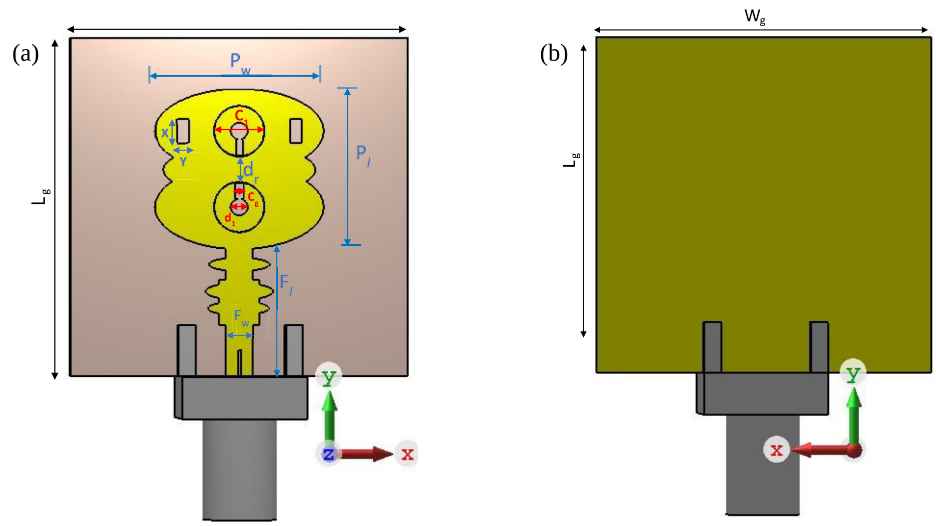

FIGURE 1. Proposed antenna geometry in a single port. (a) Front view and (b) ground view.

relation coefficient (ECC), diversity gain (DG), total active reflection coefficient (TARC), and mean effective gain (MEG), together with comparisons against representative mmWave and reported six-port MIMO antennas.

The remainder of this paper is organized as follows. Section 2 outlines the antenna design and mechanism. Section 3 discusses simulated and measured results. Section 4 evaluates MIMO performance. Sections 5 and 6 present comparative analyses with reported mmWave and six-port antennas, respectively. Section 7 concludes the paper.

2. ANTENNA DESIGN AND DEVELOPMENT

2.1. Substrate Selection and Antenna Geometry

The proposed single antenna element was designed on a Rogers RT/duroid® 5880 substrate with a relative permittivity of $\varepsilon_r = 2.2$, thickness of $h = 0.508$ mm, and loss tangent of $\tan\delta = 0.0009$. The single-port antenna was excited through a $50\,\Omega$ microstrip feed line, with overall dimensions of $L_g \times W_g \times h_g$ mm^3 and a full ground plane, where $h_g = 0.543$ mm, as shown in Fig. 1. The antenna element was first optimized near 39.15 GHz before being extended to the six-port MIMO configuration. Table 2 shows the clear dimensions of the single-port antenna. Each radiating element consists of a modified square patch with a small slot introduced for resonance tuning.

The substrate dimensions were calculated using the following equations: The initial geometrical dimensions of the proposed antenna were estimated using standard microstrip antenna design relations. The parameters W_g, $\varepsilon_{\mathit{eff}}$, and L_g provide the antenna's basic dimensional framework before introducing an optimized slot-loaded radiating structure. These equations are useful for obtaining a reliable starting point for the substrate/ground size and the antenna's effective electrical length.

The ground width is calculated as:

$$W_g = \frac{C}{2f_l\sqrt{\frac{\varepsilon_r+1}{2}}} \tag{1}$$

TABLE 2. Single-element antenna geometry parameters.

Parameters	Dimension (mm)	Parameters	Dimension (mm)
W_g	20	X	1.4
L_g	20	Y	0.7
P_w	10	d_r	1.49
P_l	10	C_1	3 (diameter)
F_l	8	C_g	0.4
F_w	1.6	d_1	0.5

where f_l represents the lower operating frequency, and ε_r is the relative permittivity of the substrate. The proper selection of W_g is important because the ground plane influences impedance matching, current distribution, and radiation stability. In the proposed MIMO antenna, W_g also contributes to maintaining compactness while supporting the required 5G mmWave operating band.

The effective dielectric constant is approximated as:

$$\varepsilon_{\mathit{eff}} = \frac{\varepsilon_r+1}{2} + \frac{\varepsilon_r-1}{2}\left(1+\frac{12h}{W}\right)^{-1/2} \tag{2}$$

The parameter $\varepsilon_{\mathit{eff}}$ represents the effective medium experienced by the electromagnetic wave because the fringing fields are distributed partly on the substrate and partly in air. Therefore, $\varepsilon_{\mathit{eff}}$ is more suitable than directly using ε_r for estimating the antenna's guided wavelength and electrical length, where 'c' corresponds to the speed of light in vacuum ($= 3\times10^8$ m/s).

The ground-plane length L_g is calculated as

$$L_g = \frac{f_0}{2f_l\sqrt{\varepsilon_{\mathit{eff}}}} - 0.824h_s\left(\frac{(\varepsilon_{\mathit{eff}}+0.30)\left(\frac{W_1}{h_g}+0.264\right)}{(\varepsilon_{\mathit{eff}}-0.258)\left(\frac{W_1}{h_g}+0.80\right)}\right) \tag{3}$$

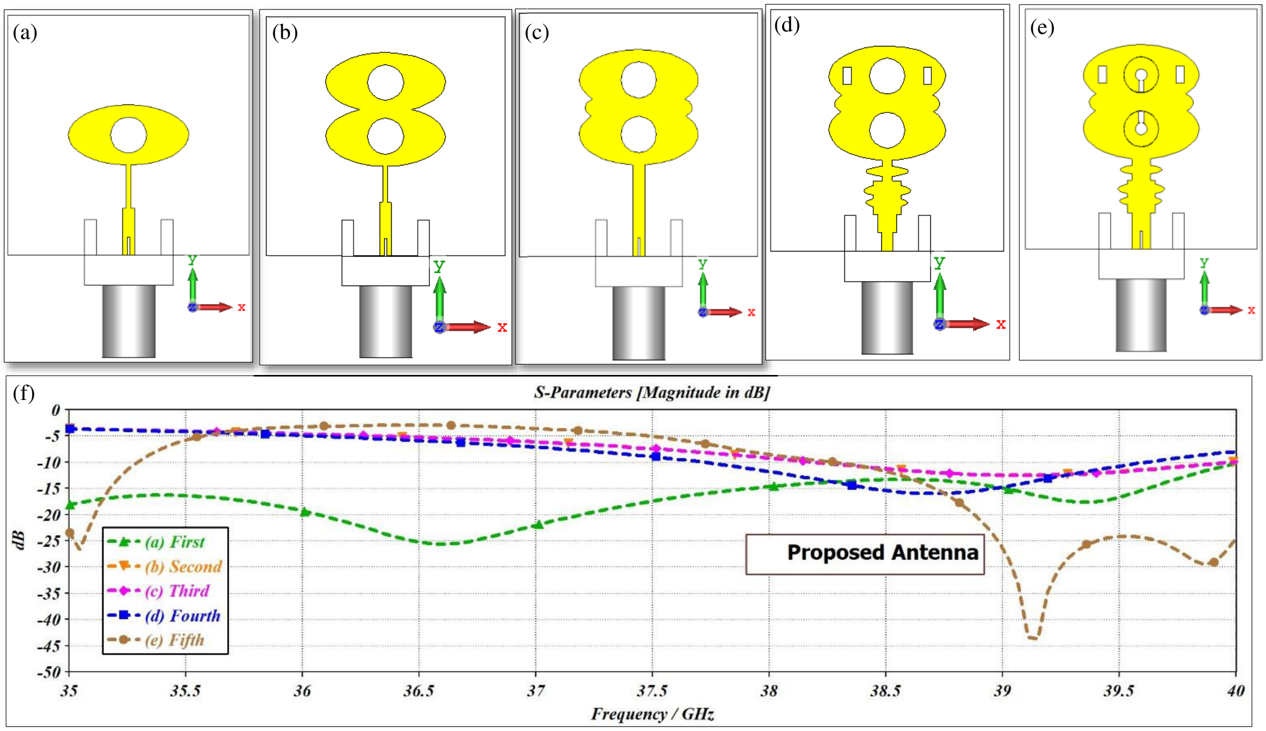

FIGURE 2. Evolution of proposed MIMO antenna: (a) single feed, (b) loop feed, (c) effective feed, (d) edge feed, (e) final resonating feed, and (f) return loss (S_{11}) dB of all the evolution MIMO.

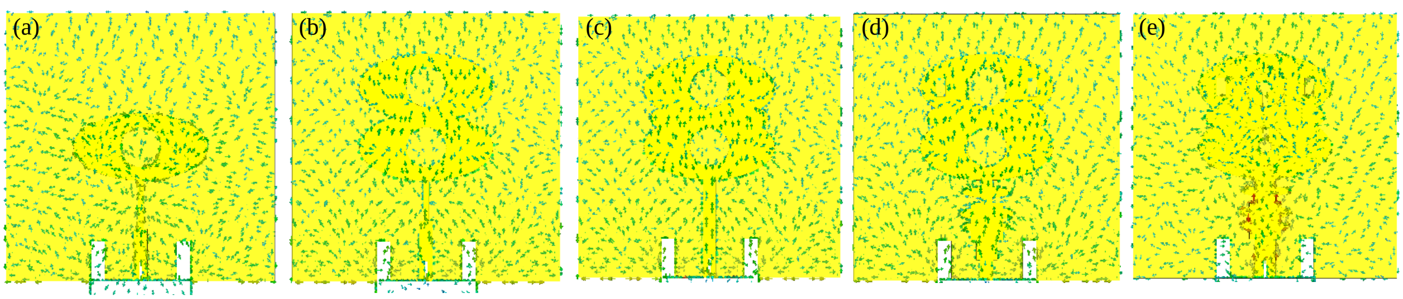

FIGURE 3. Surface current distributions illustrating the electromagnetic evolution of the proposed antenna during successive design stages (a)–(e) at 39 GHz.

2.2. S-Parameter-Based Optimization

Figure 2 illustrates the electromagnetic (EM) evolution through configurations (a)–(e). The baseline radiator (a) provides a moderate initial match. Structural modifications in (b), (c), and (d) — incorporating multi-loop coupling, structural asymmetries, and a meandered stepped feed — alter the surface current paths but introduce significant parasitic reactance ($X_{parasitic}$). This shifts the input impedance ($Z_{in} = R_{in} + jX_{in}$) away from the 50 Ω characteristic impedance (Z_0) as shown in Fig. 16(a), degrading the intermediate S_{11} curves between 35 and 38.5 GHz as defined by:

$$S_{11} = \left(\frac{Z_{in} - Z_0}{Z_{in} + Z_0} \right) \quad (4)$$

In the optimized proposed antenna (e), strategically etched internal slots and cut-outs introduce a compensatory reactance (X_{slots}) that neutralizes the accumulated parasitics ($X \approx 0$) and restores $R_{in} \approx 50\,\Omega$. This precise conjugate match yields highly efficient, deep resonances at 39.1 GHz (-44 dB), ensuring optimal operation for 5G mmWave applications.

Figure 3 illustrates the evolution of the surface current distribution for each design stage, providing physical insight into underlying resonant mechanisms. The progressive redistribution of the current path enhances feed-to-radiator coupling, extends effective electrical length, and excites additional resonant modes, leading to improved impedance matching and broader operating bandwidth. The electromagnetic role and corresponding performance improvement of each structural modification are summarized in Table 3, confirming the proposed antenna's design rationale.

2.3. Six-Port MIMO Antenna Configuration

In Fig. 4(a), the geometric layout and port configuration of the proposed six-port MIMO antenna system are designed using

TABLE 3. Electromagnetic evolution and design rationale of the proposed antenna.

Stage	Design Modification	Electromagnetic Mechanism	Resulting Performance
(a)	Initial radiator	Supports a single dominant current path with limited electrical length, resulting in weak resonance within the desired frequency band.	Initial resonant response with poor impedance matching.
(b)	Addition of the second circular radiator	Introduces an additional coupled current path, increasing the effective electrical length and exciting a second resonant mode.	Improved impedance matching and enhanced operating bandwidth.
(c)	Edge contouring and slot incorporation	Redistributes the surface current and modifies the current path, leading to improved resonance stability and impedance characteristics.	Enhanced bandwidth and improved resonance alignment toward the target frequency band.
(d)	Meandered microstrip feed	Enhances electromagnetic coupling between the feed line and the radiator while improving impedance transformation.	Improved impedance matching and resonance shifted toward the desired operating frequency.
(e)	Final slotted radiator with circular perturbations	Establishes multiple coupled resonant current paths and improves current confinement within the radiating structure, resulting in stable electromagnetic behavior.	Wide operating bandwidth, deep impedance matching, and stable radiation characteristics across the 35–40 GHz frequency band.

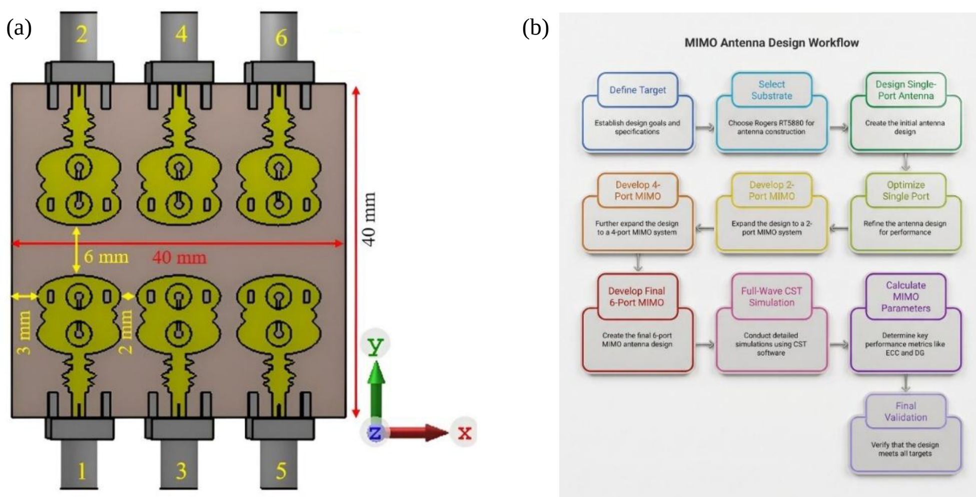

FIGURE 4. Evolution of proposed MIMO antenna: (a) Six-port MIMO with minimum dimensions and (b) Flowchart for design flow of proposed MIMO.

the Computer Simulation Technology (CST) model. The architecture consists of six symmetric, modified slotted radiators arranged in a compact, face-to-face 1×3 topology on a $40 \times 40\,\text{mm}^2$ substrate footprint.

The individual elements integrate corrugated boundaries and nested slot loops to optimize electrical length and impedance bandwidth. Critical dimensional boundaries for mutual coupling suppression are highlighted, including an inter-subarray isolation gap of 6 mm, an intra-element spacing of 2 mm, and an outer edge clearance of 3 mm.

Figure 4(b) illustrates the design methodology of the proposed six-port antenna. The process begins with the 38–40 GHz design target, followed by substrate selection, single-element design, S-parameter optimization, and progressive integration into two-port, four-port, and final six-port MIMO configurations. At each stage, impedance matching, isolation, ECC, DG, TARC, and MEG were evaluated, and the geometry was refined to achieve the desired MIMO performance. The final design demonstrates compact six-port operation with stable matching, isolation, gain, and diversity characteristics across the target band.

2.4. Equivalent Circuit Validation

This equation models the impedance-matching behavior. The series combination R_f and L_f represents the microstrip feed line. The shunt capacitance C_g accounts for the coupling gap, while the series L_r-R_r network and shunt C_r model the electrical characteristics of the main patch radiator. In Fig. 5(a),

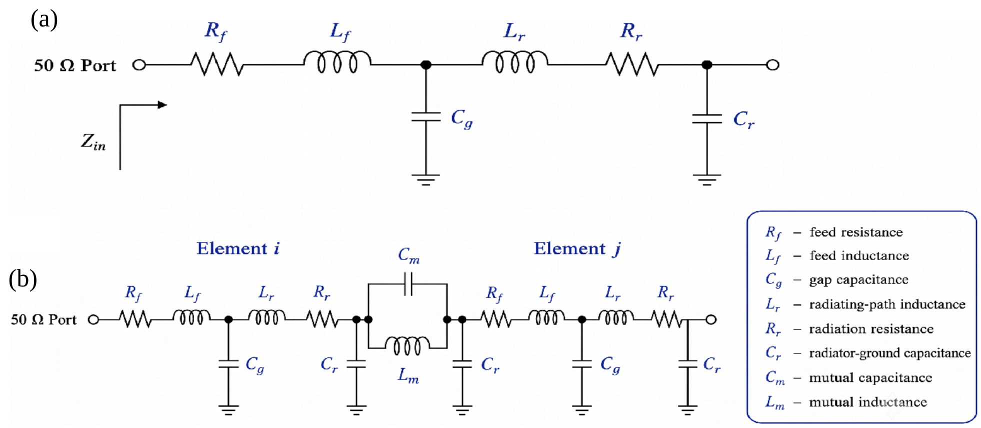

FIGURE 5. Equivalent circuit model of the proposed six-port MIMO antenna: (a) Single-element circuit model and (b) mutual-coupling model between adjacent antenna elements.

TABLE 4. Key simulation settings for the proposed MIMO antenna.

Parameter	Setting	Parameter	Setting
Solver	Time-domain S-parameter solver	Boundary condition	Expanded open boundary
Frequency range	0.1–42 GHz	PML	Four-layer convolution PML
Target operating band	38–40 GHz	Symmetry	Not used
Frequency samples	1001 linear steps	Mesh type	Hexahedral PBA mesh
Number of ports	Six waveguide ports	Mesh cells	∼29.88 million
Port mode	TEM mode	Convergence criterion	−40 dB steady-state accuracy
Port impedance	∼49.5 Ω	Extracted data	S-parameters, isolation, ECC, DG, TARC, MEG

the total input impedance looking into a single port is derived by combining the series feed network and the parallel resonator branches:

$$Z_{in} = (R_f + j\omega L_f) + \frac{1}{j\omega C_g + \frac{1}{(R_r + j\omega L_r) + \frac{1}{j\omega C_r}}} \tag{5}$$

In Fig. 16(b), the self-decoupling mechanism between adjacent elements (i and j) is determined by the parallel tank circuit formed by mutual components:

$$Z_m = \frac{j\omega L_m}{1 - \omega^2 L_m C_m} \tag{6}$$

This equation explains the high inter-port isolation (> 19 dB). The parallel LC tank circuit (L_m, C_m) represents the near-field reactive coupling between the counter-facing elements. At the operating frequency of 39.4 GHz, this parallel combination creates a parallel resonance condition (high spatial impedance block), effectively choking surface currents and preventing energy transfer to the adjacent port without requiring external decoupling structures.

For minimum coupling, $Z_{21} \to 0$

$$\omega^2 L_m C_m \approx 1 \tag{7}$$

The extracted lumped-element values for each antenna element are $R_f = 50\,\Omega$, $L_f = 0.06$ nH, $C_g = 24$ fF, $L_r = 0.17$ nH, $R_r = 105\,\Omega$, and $C_r = 92$ fF. The mutual inductance (L_m) and mutual capacitance (C_m) represent electromagnetic coupling between adjacent elements and are optimized during circuit extraction to match the full-wave simulated response of the equivalent circuit shown in Fig. 5.

3. EXPERIMENTAL AND SIMULATION METHODOLOGY

3.1. Full-Wave Simulation Setup

The proposed MIMO antenna was simulated in CST Microwave Studio 2018 using the time-domain solver, as shown in Fig. 4(a). The complete six-port scattering matrix was extracted over 0.1–42 GHz with 1001 frequency samples, covering the 38–40 GHz operating band. Six waveguide ports were assigned to radiating elements, yielding an extracted impedance of approximately 49.5 Ω, which is close to the standard 50 Ω reference value, as summarized in Table 4.

To emulate free-space radiation, expanded open boundaries with four-layer convolutional PMLs (Perfectly Matched Layer) were employed. The full proposed MIMO structure was analyzed without symmetry conditions using a hexahedral PBA (Perfect Boundary Approximation) mesh comprising approximately 29.88 million cells. Convergence was achieved using a −40 dB steady-state accuracy criterion, ensuring accurate extraction of the antenna characteristics.

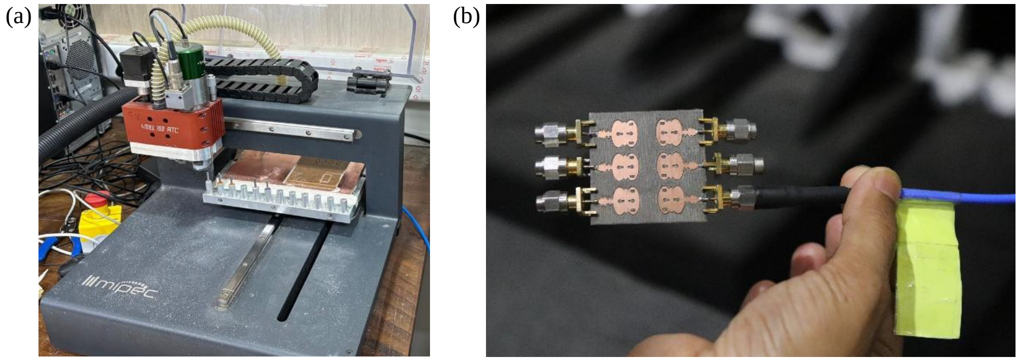

FIGURE 6. Fabrication and measurement setup of the proposed six-port MIMO antenna: (a) Fabricated prototype and (b) experimental measurement arrangement.

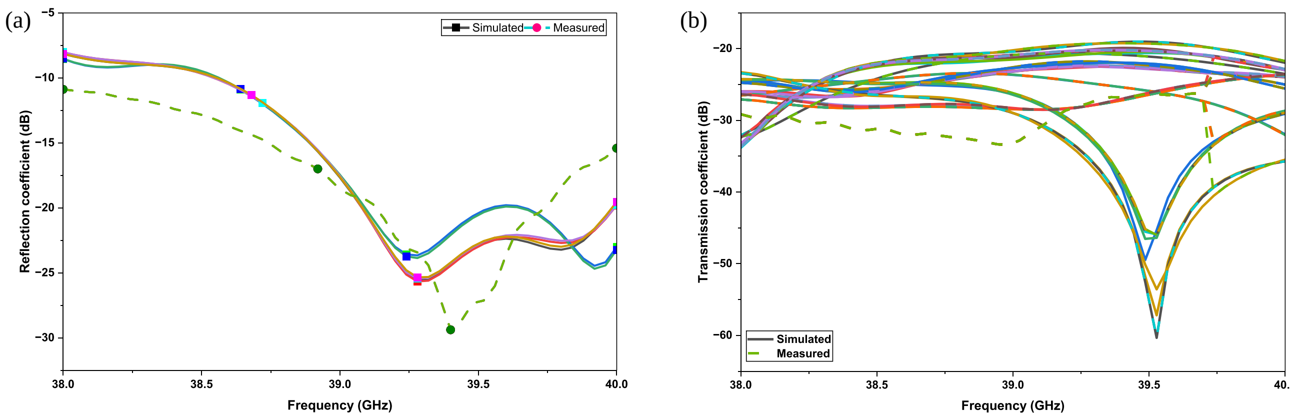

FIGURE 7. Simulated and measured S-parameter performance: (a) Reflection coefficients ($S_{xx} = S_{11}$–S_{66}) and (b) transmission coefficients (S_{xy}).

3.2. Fabrication and Measurement Setup

The optimized six-port MIMO antenna array was fabricated on a Rogers RT/duroid 5880 substrate using standard photolithographic printed circuit board (PCB) processing (Fig. 6(a)). Fabrication tolerance for the copper patch layer and feedline widths is strictly maintained within ± 0.3 mm, while the substrate thickness variation is limited to $\pm 10\%$. S-parameters were characterized using a high-performance mmWave Vector Network Analyzer (VNA) by sequentially exciting a single port while terminating all unexcited ports with matched 50 Ω loads. Far-field radiation patterns and realized gain were experimentally characterized inside the ETS-Lindgren combined Near-Field/Far-Field Tapered Anechoic Chamber facility at ISRO's Space Applications Centre (SAC), Ahmedabad (Fig. 6(b)).

The chamber provides a highly isolated quiet zone operating up to 40.0 GHz, and a standard WR-28 gain horn antenna was used as the reference calibration standard. The experimental data successfully validate the simulated impedance bandwidth, inter-port isolation (≤ -19 dB), and radiation profiles. Minor discrepancies in resonance depth and transmission ripples are strictly attributed to sub-mm fabrication tolerances, SMA precision 2.92 mm (K-type) end-launch RF connectors, and localized substrate dielectric variations at the 38.0–40.0 GHz mmWave band.

4. RESULTS AND DISCUSSION

4.1. Simulated and Measured S-parameter Performance

Figure 7 shows simulated and measured S-parameters of the proposed six-port MIMO antenna array. Simulated S_{11}–S_{66} overlap, confirming structural symmetry and stable impedance matching (≤ -10 dB) across 38–40 GHz with a resonance at 39.4 GHz (simulated $S_{xx} \approx -25.6$ dB). Measured S_{xx} for all six ports tracks closely and exhibits a resonant notch at 39.4 GHz with a depth of ≈ -29 dB, indicating negligible frequency shift. Simulated worst-case inter-port coupling (S_{xy}) is below -19 dB; measured S_{xy} similarly remains < -19 dB, confirming that the optimized spacing and counter-facing arrangement provide intrinsic isolation without external decoupling. Minor differences in return-loss depth are attributed to connector soldering tolerances (2.92 mm K-type), fabrication tolerances, substrate dielectric loss and dispersion, conductor surface roughness, and VNA measurement uncertainty at mmWave frequencies.

4.2. Radiation and Total Efficiency Analysis

Figure 8 presents the simulated radiation efficiency (η_{rad}) and total efficiency (η_{tot}) of the proposed six-port MIMO antenna over the 38–40 GHz operating band. All antenna elements exhibit stable efficiency characteristics, with a slight improve-

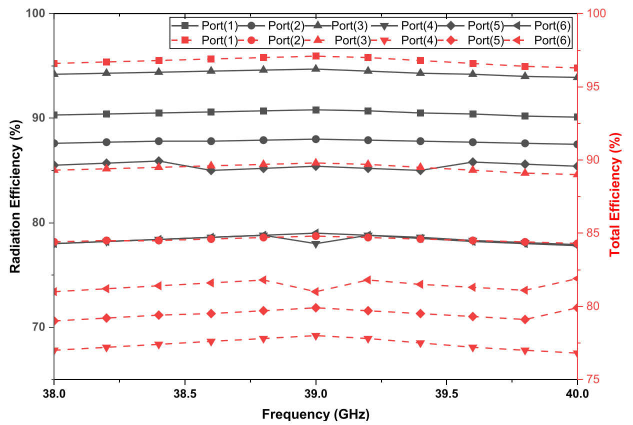

FIGURE 8. Simulated radiation efficiency (η_{rad}) and total efficiency (η_{tot}) variations across the operating frequency.

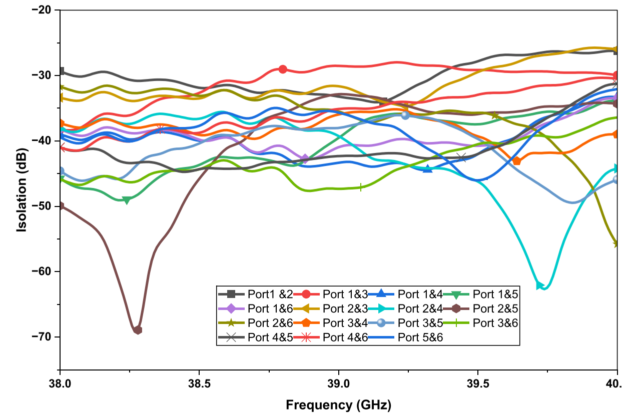

FIGURE 9. Measured isolation characteristics of the proposed six-port MIMO antenna.

ment near the design frequency of 39 GHz. Owing to the compact array configuration and the non-identical coupling environments experienced by each radiating element, minor variations are observed among the ports. The radiation efficiency ranges from 84.3% to 97.1%, with Port 2 achieving the highest efficiency and Port 4 the lowest value. The total efficiency, which accounts for radiation loss, dielectric and conductor losses, and impedance mismatch, follows a similar frequency-dependent trend and varies from 76.8% to 85.9% across the operating band. The limited efficiency variation over the 2 GHz bandwidth demonstrates effective impedance matching, low dissipative losses, and balanced multi-port operation. These results verify that the proposed antenna maintains high radiation performance and is well-suited for high-capacity 5G mmWave MIMO communication systems.

4.3. Inter-Port Isolation Analysis

Measured isolation characteristics of the proposed six-port MIMO antenna array are shown in Fig. 9. The distance between elements is 2 mm ($\approx 0.26\lambda_0$ at 39 GHz), and the distance between the upper and lower antenna groups is 6 mm ($\approx 0.78\lambda_0$), leading to a compact configuration. However, the counter-facing arrangement, optimized inter-element spacing, and symmetric grounding help suppress mutual coupling even though the spacing is tight. Most port pairs have transmission coefficients less than -25 dB over the operating band, and isolation is greater than -40 dB at some frequencies. The results show that the geometrical configuration of the array and the resulting distribution of the electromagnetic field suppress surface-wave propagation and near-field coupling among nearby radiators, allowing for multiport isolation without additional decoupling networks and suggesting its appropriateness for compact 5G mmWave MIMO applications shown in Fig. 10.

4.4. Surface Current Distribution

Figures 10(a)–(f) present surface-current distributions of the proposed six-port MIMO antenna when each antenna element is excited individually, and the remaining ports are terminated with 50 Ω loads. A consistent current distribution is observed for all excitation cases, confirming that the isolation mechanism is independent of the excited port. Despite the compact edge-to-edge spacing of only 2–3 mm, the current remains predominantly confined to the excited radiator and its feed, whereas only weak induced currents are observed on adjacent elements. This current confinement minimizes near-field overlap between neighbouring radiators, thereby reducing the mutual impedance responsible for inter-element coupling. Furthermore, the mirrored arrangement of the upper and lower antenna rows spatially separates regions of the maximum current density, further weakening electromagnetic interaction between adjacent elements. This behaviour is corroborated by the transmission coefficients in Fig. 7, where the mutual coupling remains below -20 dB across the operating band.

4.5. Gain

Figure 11(a) presents the simulated gain of the proposed six-port MIMO antenna over the operating band. All six ports exhibit stable gain characteristics with only minor variations, reflecting the effects of mutual coupling and current redistribution in the compact MIMO configuration. Fig. 11(b) compares the simulated and measured peak gains at 39.25 GHz. The measured peak gain of 8.28 dBi, obtained using the reference antenna method from the H-plane maximum, shows good agreement with the simulated results. The slight deviation is primarily attributed to fabrication tolerances, connector and transition losses, dielectric property variations, conductor surface roughness, and measurement uncertainty at mmWave frequencies.

4.6. MIMO Diversity Performance

The MIMO performance was evaluated using ECC, DG, TARC, and MEG, which characterize the correlation, diversity, active reflection, and power balance of the proposed antenna.

4.6.1. ECC and Diversity Gain

Figure 12 compares simulated and measured ECCs and DGs of the proposed MIMO antenna. Across the 38–40 GHz band,

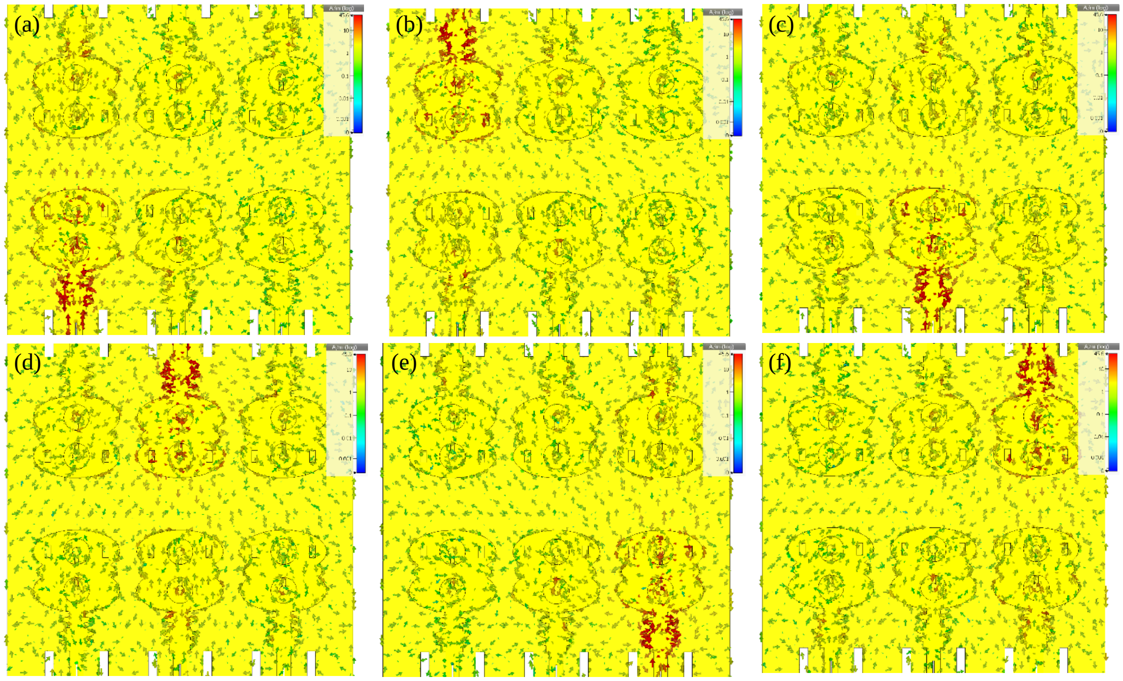

FIGURE 10. Surface current distributions of the proposed six-port MIMO antenna at 39 GHz with individual port excitation while the remaining ports are terminated with 50 Ω loads: (a) Port 1, (b) Port 2, (c) Port 3, (d) Port 4, (e) Port 5, and (f) Port 6.

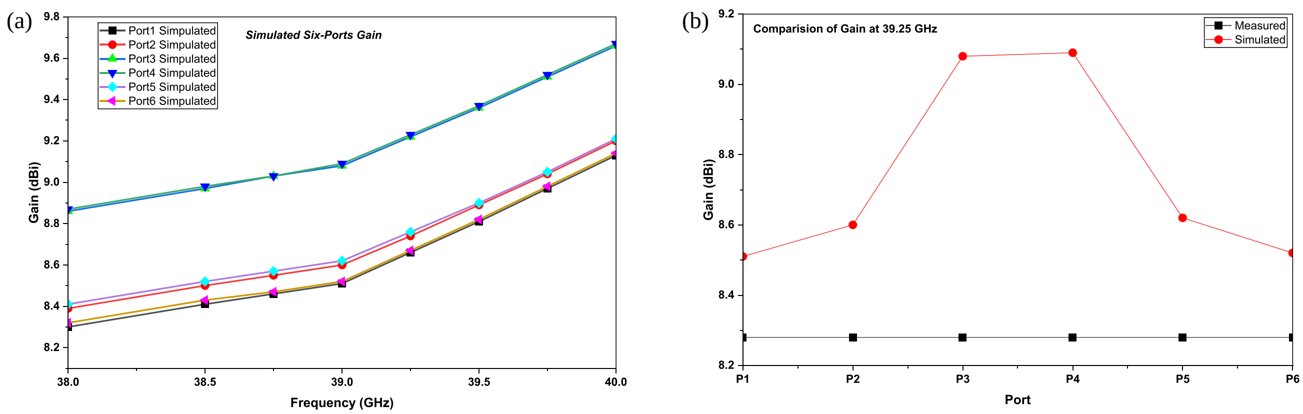

FIGURE 11. Gain characteristics of the proposed six-port MIMO antenna: (a) Simulated gain over the 38–40 GHz operating band for all six-port and (b) Comparison of simulated and measured peak gains at 39.25 GHz.

simulated and measured ECCs remain below 2.5×10^{-3}, with minimum values of approximately 5×10^{-4} and 4×10^{-4}, respectively, near 39.5 GHz. These values are well below the accepted limits of 0.5 and 0.01, confirming excellent diversity performance and low correlation between antenna elements.

For a two-port pair, the ECC can be calculated from S-parameters as follows:

$$\mathrm{ECC}_{ij} = \frac{\left|S_{ii}^{*} S_{ij} + S_{ji}^{*} S_{jj}\right|^{2}}{\left(1 - |S_{ii}|^{2} - |S_{ji}|^{2}\right)\left(1 - |S_{jj}|^{2} - |S_{ij}|^{2}\right)} \tag{8}$$

The low ECC values result in a DG close to 10 dB across the operating band, indicating excellent diversity performance. Minor differences between the simulated and measured ECC and DG results are attributed to fabrication and measurement tolerances.

DG is related to ECC as:

$$\mathrm{DG} = 10\sqrt{1 - |\mathrm{ECC}|^{2}} \tag{9}$$

4.6.2. Diversity Performance Analysis (Envelope Correlation Coefficient)

To rigorously evaluate multi-port diversity performance and independent channel operation of the proposed MIMO antenna system, the envelope correlation coefficient (ρ_e) is investigated. While S-parameter-based ECC calculations provide a quick estimation, they neglect the real-world radiation mechanism and dielectric/conduction losses. Therefore, the far-field radiation-pattern-based ECC is computed over the spatial angular sphere using the 2D integrated field approach described

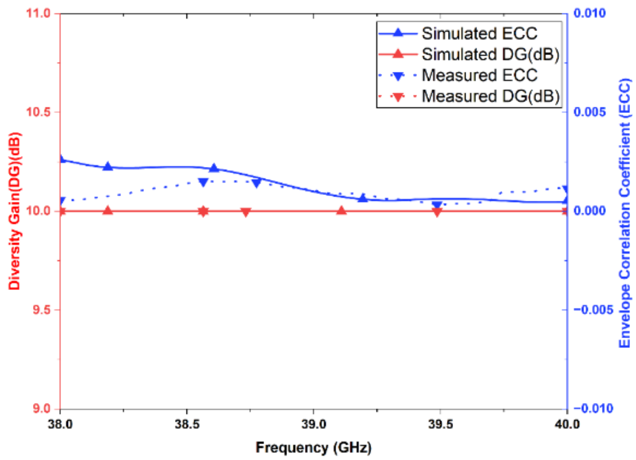

FIGURE 12. Simulated and measured ECC and DG performance of the proposed MIMO antenna.

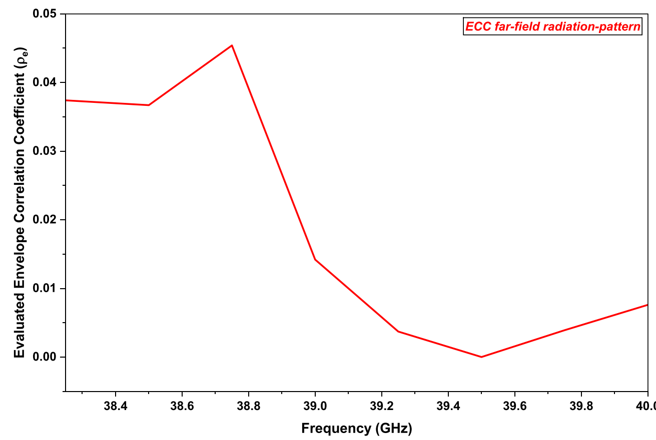

FIGURE 13. Evaluated envelope correlation coefficient (ρ_e) as a function of frequency across the targeted operational band.

by:

$$\rho_e = \frac{\left|\int_{-90}^{+90} E_1(\theta)E_2^*(\theta)\, d\theta\right|^2}{\left[\int_{-90}^{+90} |E_1(\theta)|^2\, d\theta\right]\left[\int_{-90}^{+90} |E_2(\theta)|^2\, d\theta\right]} \tag{10}$$

where $E_1(\theta)$ and $E_2(\theta)$ represent the measured 2D co-polar far-field electric field distributions of Port 1 and Port 2, respectively.

The spatial overlap parameters, phase distributions, and power variations across the complete angular sweep ($\theta = -90^\circ$ to $+90^\circ$) were extracted and integrated at the primary mmWave operating design frequency. At the exact operational frequency of 39.25 GHz, the computed space-integrated ECC value settles at 0.0037. As shown in Fig. 13, the envelope correlation, which remains well below 0.004 across the band, indicates an exceptionally low correlation profile. Because this result is substantially lower than the universal industrial threshold of $\rho_e < 0.5$, it mathematically confirms excellent pattern diversity. The positive and negative phase variations effectively cancel out across the spatial integration, demonstrating that the multi-port configuration maintains outstanding mutual isolation and preserves total channel capacity without performance degradation.

4.6.3. Total Active Reflection Coefficient

Figure 14 compares the simulated and measured TARC responses of the proposed MIMO antenna. TARC characterizes the active reflection performance under simultaneous multi-port excitation by accounting for mutual coupling and the combined reflected power from all ports.

For an N-port MIMO antenna, the TARC is expressed as:

$$\Gamma_a^t = \sqrt{\frac{\sum_{i=1}^{N} |b_i|^2}{\sum_{i=1}^{N} |a_i|^2}} \tag{11}$$

where a_i and b_i are the incident and reflected waves at the ith port, respectively. For the proposed antenna, $N = 6$. The TARC in decibels is given by:

$$\text{TARC (dB)} = 20 \log_{10}(\Gamma_a^t) \tag{12}$$

The simulated and measured TARC responses exhibit similar trends, reaching approximately -12.5 dB and -13 dB, respectively, near 39.7 GHz. The TARC remains predominantly below -10 dB across the primary bandwidth. The slight degradation near the upper-band edge is attributed to the intense near-field coupling inherent in the highly compact 2 mm element spacing, representing a practical trade-off between miniaturization and active impedance matching. Overall, the measured results validate the active impedance stability of the proposed MIMO antenna. Fig. 14(b) presents the TARC of the proposed six-port MIMO antenna system evaluated across 10,000 independent, uniformly distributed random phase combinations (θ_2, θ_3, θ_4, θ_5, $\theta_6 \in [0, 2\pi]$) with Port 1 serving as the phase reference ($\theta_1 = 0^\circ$). This comprehensive statistical sweep evaluates the operational stability of the multi-port system under dynamic, non-ideal operating conditions, outlining the absolute boundaries of performance through the best-case, mean, and worst-case envelopes.

4.6.4. Mean Effective Gain

Figure 15 shows the simulated and measured MEG responses of the six ports and the maximum MEG imbalance. The MEG evaluates the average received power of each antenna element in a multipath environment and is useful for verifying the power balance among MIMO ports.

The MEG of the ith port is expressed as:

$$\text{MEG}_i = \frac{1}{2}\left(1 - \sum_{j=1}^{N} |S_{ij}|^2\right) \tag{13}$$

The maximum MEG imbalance is defined as:

$$\Delta\text{MEG}_{\max} = |\text{MEG}_i\,(\text{dB}) - \text{MEG}_j\,(\text{dB})| \tag{14}$$

The MEG values of all six ports remain closely matched, varying from approximately -3.75 to -3.10 dB across the operating band. The measured results closely follow the simu-

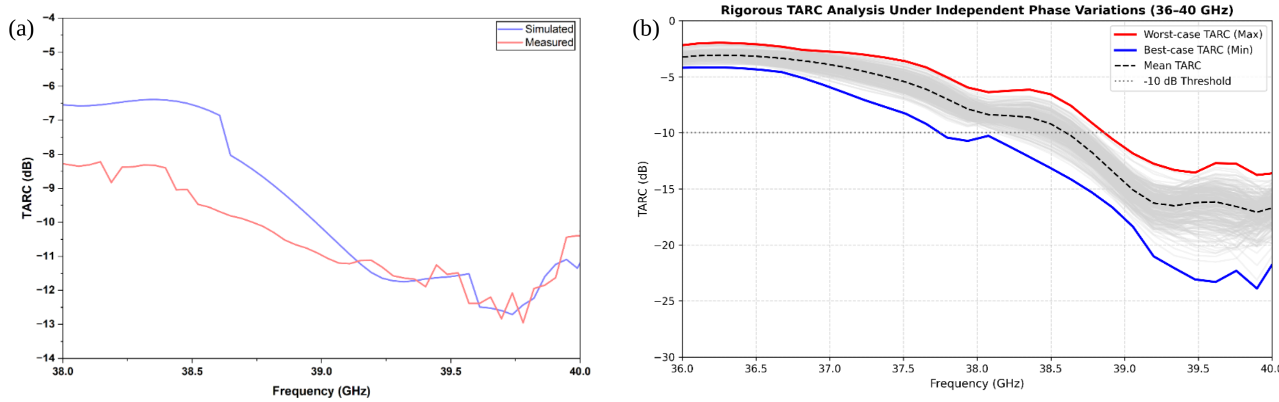

FIGURE 14. TARC. (a) Simulated and measured performance of the proposed MIMO antenna and (b) simulated TARC curves under 10,000 independent phase distributions across the six ports.

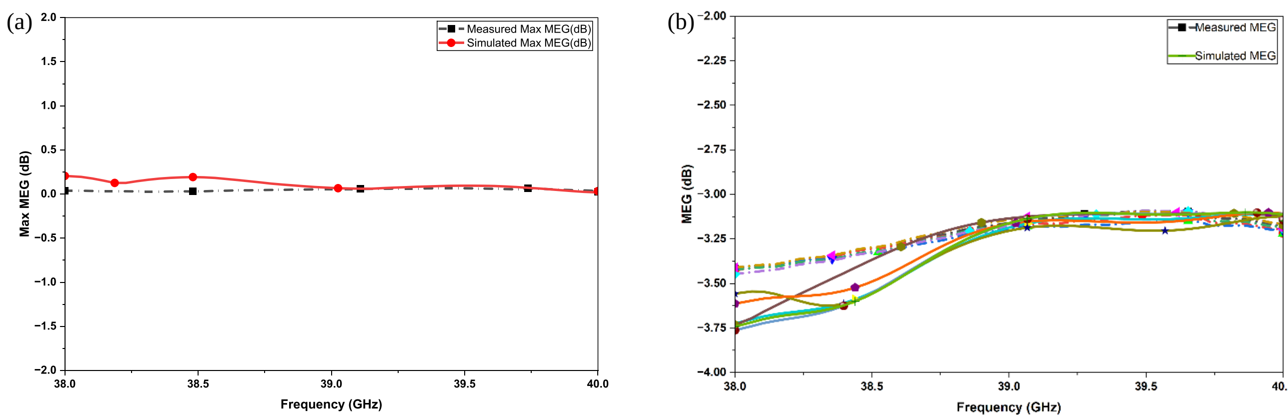

FIGURE 15. MEG performance of the proposed MIMO antenna: (a) Maximum MEG imbalance and (b) simulated and measured MEGs of individual ports.

lated trend, with the maximum MEG imbalance remaining well within the accepted 3 dB limit. These results confirm balanced power reception and reliable diversity performance of the proposed MIMO antenna.

5. ANALYTICAL MODELING VALIDATION

An equivalent circuit model was developed to explain the resonance and impedance-matching behavior of the proposed antenna, as shown in Fig. 5. The feed line, radiator, and coupling gaps are represented by equivalent RLC elements, with resonance governed by the effective LC response $f_r = 1/(2\pi\sqrt{LC})$. At resonance, the inductive and capacitive reactances cancel, yielding an input impedance close to $50\,\Omega$ feed condition. In the proposed MIMO configuration, inter-element coupling is modeled using mutual capacitance and inductance. The close agreement between the equivalent circuit and full-wave responses in the 38–40 GHz band validates the dominant resonance mechanism, while minor deviations arise from the lumped-element approximation and neglected distributed-field effects.

As depicted in Figs. 16(a) and (b), the proposed six-port MIMO antenna was experimentally validated at the Space Applications Centre (SAC), ISRO, Ahmedabad, India. Impedance characteristics were captured using a passive SOLT (Short-Open-Load-Through)-calibrated Anritsu S820E Vector Network Analyzer (VNA). Far-field anechoic chamber evaluations yielded highly reliable results, maintaining uncertainties of ± 0.5 dB for gain and ± 3 dB for cross-polarization (down to the -30 dB level), rigorously demonstrating the design's feasibility for 38–40 GHz 5G mmWave applications.

6. PERFORMANCE COMPARISON WITH REPORTED SIX-PORT MIMO ANTENNAS

In Table 5, several six-port MIMO antennas have been reported for mmWave applications. Rahman et al. [34] presented a 3D tri-band design, while Jayanthi and Kalpana [35] proposed a dual-band 28/38 GHz antenna using parasitic elements. Shariff et al. [36] employed a decoupling structure to enhance isolation, and Ahmad and Hashmi [37] used a hybrid DGS-FSS approach. In contrast, the proposed antenna realizes a compact planar six-port MIMO configuration operating across 38–40 GHz without DGS, FSS, metasurfaces, or additional decoupling networks, while maintaining isolation above 20 dB, very low ECC, DG close to 10 dB, balanced MEG, and acceptable TARC performance.

(a)

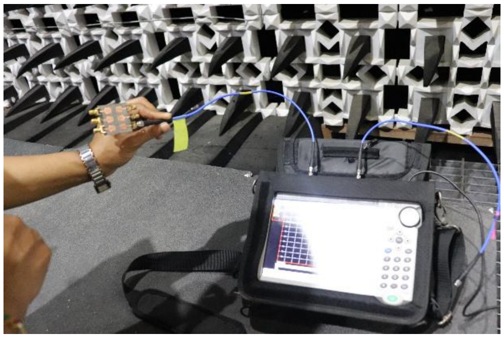

(b)

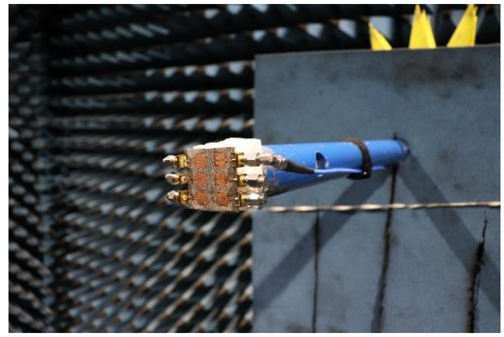

FIGURE 16. Antenna measurement setup. (a) VNA test samples and (b) anechoic chamber measurement setup of the proposed six-port MIMO antenna.

TABLE 5. Comparison of existing six-port MIMO antennas for 5G applications for 38–40 GHz.

Ref.	Material/Substrate	Overall dimensions (mm)	Gain (dBi)	Isolation (dB)	ECC	Decoupling Technique
[34]	Rogers RT5880	$70 \times 70 \times 70$	7.5	max. nearly 50	< 0.004	Patch + Parasitic Elements (3D Orthogonal Configuration)
[35]	Rogers RT/Duroid 5880	$50 \times 35 \times 0.8$	10.09	better than 20	< 0.01	Geometry-based decoupling
[36]	Rogers RT5880	$15 \times 24 \times 0.79$	7.2	> 20	Measured < 0.45;	Open-ended decoupling structure
[37]	Rogers RT5880	$1.97 \times 3.39\lambda^2$	8.77	33	Far-field < 0.02; realistic Gaussian model < 0.04	FSS + DGS
Proposed work	**Rogers RT5880**	$\mathbf{40 \times 40 \times 0.543}$	**8.28**	$\mathbf{> 20}$	$\mathbf{5 \times 10^{-4}}$	**Self-decoupled design**

In contrast to many reported six-port mmWave MIMO antennas, which achieve high isolation through auxiliary decoupling structures or increased inter-element spacing, the proposed antenna achieves intrinsic isolation via an optimized radiator topology and a symmetric element arrangement. This self-decoupled design enables a compact six-port MIMO configuration with only 2–3 mm edge-to-edge spacing while maintaining an inter-element isolation exceeding 20 dB, without employing defected ground structures (DGS), electromagnetic bandgap (EBG) structures, neutralization lines, parasitic elements, or external decoupling networks. Furthermore, the proposed approach reduces structural complexity while offering a compact footprint of 40×40 mm^2, an ultra-thin profile of 0.543 mm, and favorable MIMO characteristics, making it suitable for highly integrated 5G mmWave applications.

7. CONCLUSION

This paper has presented a compact planar six-port MIMO antenna covering the 38–40 GHz mmWave band on a Rogers RT5880 substrate with overall dimensions of $40 \times 40 \times 0.543$ mm^3. Simulated and measured results demonstrated good impedance matching throughout the operating band, with a dominant resonance near 39.3–39.5 GHz and close agreement between simulation and measurement. The proposed antenna achieved inter-port isolation exceeding 20 dB without requiring additional decoupling structures. MIMO performance was validated by an ECC of 5×10^{-4}, a DG close to 10 dB, acceptable TARC, and balanced MEG, confirming low correlation and excellent diversity characteristics. The measured gain remained stable across the operating band, verifying reliable radiation performance. Compared with existing six-port mmWave MIMO antennas, the proposed design offers a compact planar architecture with experimentally validated performance in the 38–40 GHz band. Future work will investigate the integration of EBG cells, frequency-selective surfaces, metasurfaces, dielectric lenses, and passive reflectors to further enhance isolation, gain, radiation efficiency, and beam control for next-generation mmWave MIMO systems.

ACKNOWLEDGEMENT

The authors would like to express their sincere gratitude to Dr. Ravinder Kumar, Scientist, Central Research Facility, IIT Delhi, for his valuable support in providing access and time slots for the preparation of the proposed antenna. His technical assistance and facility support were highly beneficial for prototype-related work.

The authors also gratefully acknowledge Mr. Dharmendra Singh, Scientist/Engineer, Antenna Systems Area, Space Applications Center (SAC), ISRO, Ahmedabad, for providing support and access to slots for obtaining the analytical results of the proposed antenna. His guidance and technical cooperation significantly contributed to the validation and strengthening of this research.

The authors sincerely appreciate the support extended by both institutions and individuals in facilitating the successful completion of this study.

REFERENCES

[1] Faniar, A. A. M., A. A. Almohammedi, and M. Balfaqih, "Advancements in millimeter wave MIMO antenna arrays for enhanced 5G connectivity," in *2023 28th Asia Pacific Conference on Communications (APCC)*, 424–429, Sydney, Australia, 2023.

[2] Raj, T., R. Mahapatra, A. P. Das, M. Sahoo, R. Mishra, and H. Pradhan, "A compact ultra-wideband planner MSA for mmWave FR-II NR: n257, n258, n262 and n260 bands for 5G wireless applications," in *2024 Second International Conference on Microwave, Antenna and Communication (MAC)*, 1–6, Dehradun, India, 2024.

[3] Farahat, A. E. and K. F. A. Hussein, "Dual-band (28/38 GHz) wideband MIMO antenna for 5G mobile applications," *IEEE Access*, Vol. 10, 32 213–32 223, 2022.

[4] Tsao, Y.-F., A. Desai, and H.-T. Hsu, "Dual-band and dual-polarization CPW fed MIMO antenna for fifth-generation mobile communications technology at 28 and 38 GHz," *IEEE Access*, Vol. 10, 46 853–46 863, 2022.

[5] Malik, B. T., S. Khan, J. Nasir, and S. Koziel, "Enhanced gain and isolation dual-band dual-port MIMO antenna with integrated lens for millimeter-wave 5G internet-of-things applications," *IEEE Access*, Vol. 13, 40 859–40 874, 2025.

[6] Wang, H., J. Wang, X.-X. Yang, and Q. Zheng, "Isolation and bandwidth enhancement of 5G millimeter-wave dual-band MIMO antenna based on metamaterial wall," in *2024 14th International Symposium on Antennas, Propagation and EM Theory (ISAPE)*, 1–3, Hefei, China, 2024.

[7] Desai, A., C. D. Bui, J. Patel, T. Upadhyaya, G. Byun, and T. K. Nguyen, "Compact wideband four element optically transparent MIMO antenna for mm-Wave 5G applications," *IEEE Access*, Vol. 8, 194 206–194 217, 2020.

[8] Farahat, A. E. and K. F. A. Hussein, "28/38 GHz dual-band Yagi-Uda antenna with corrugated radiator and enhanced reflectors for 5G MIMO antenna systems," *Progress In Electromagnetics Research C*, Vol. 101, 159–172, 2020.

[9] Raheel, K., A. Altaf, A. Waheed, S. H. Kiani, D. A. Sehrai, F. Tubbal, and R. Raad, "E-shaped H-slotted dual band mmWave antenna for 5G technology," *Electronics*, Vol. 10, No. 9, 1019, 2021.

[10] Addepalli, T., T. Vidyavathi, M. V. Sudhakar, C. R. Jetti, C. Swamy, S. Medasani, P. Badugu, and A. J. A. Al-Gburi, "A novel isolation-enhanced four-element high-gain hexa-band MIMO antenna for 5G mmWave systems," *Wireless Personal Communications*, Vol. 146, 663–683, 2026.

[11] Tadesse, A. D., O. P. Acharya, and S. Sahu, "A compact planar four-port MIMO antenna for 28/38 GHz millimeter-wave 5G applications," *Advanced Electromagnetics*, Vol. 11, No. 3, 16–25, 2022.

[12] Elsharkawy, R. R., K. F. A. Hussein, and A. E. Farahat, "Dual-band (28/38 GHz) compact MIMO antenna system for millimeter-wave applications," *Journal of Infrared, Millimeter, and Terahertz Waves*, Vol. 44, No. 11, 1016–1037, 2023.

[13] El Houda Nasri, N., M. E. Ghzaoui, and M. Fattah, "A quad port MIMO antenna with improved bandwidth and high gain for 38 GHz 5G applications," *Franklin Open*, Vol. 6, 100078, 2024.

[14] Addepalli, T., T. Vidyavathi, M. SatishKumar, G. Divya, M. Balaji, S. Medasani, M. S. Zidan, I. M. Ibrahim, and A. J. A. Al-Gburi, "A compact quad-element serrated boundary fractal planar antenna for multi-band mmWave 5G/6G wireless applications," *PLoS One*, Vol. 21, No. 6, e0349601, Jun. 2026.

[15] Tiwari, R. N., D. Sharma, P. Singh, and P. Kumar, "A flexible dual-band 4×4 MIMO antenna for 5G mm-Wave 28/38 GHz wearable applications," *Scientific Reports*, Vol. 14, No. 1, 14324, 2024.

[16] Alsalman, A., A. Alhumaid, A. Alnogithan, E. K. I. Hamad, and M. Shaban, "Reconfigurable 28/38 GHz wideband and high isolation MIMO antenna for advanced mmWave applications," *Journal of Electrical Engineering*, Vol. 75, No. 6, 467–483, 2024.

[17] Munir, M. E., M. M. Nasralla, and M. A. Esmail, "Four port tri-circular ring MIMO antenna with wide-band characteristics for future 5G and mmWave applications," *Heliyon*, Vol. 10, No. 8, e28714, 2024.

[18] Sethumadhavi, R., B. Mishra, A. K. Singh, D. Yadav, S. Eduru, and T. Y. Satheesha, "Dual and wideband mmWave 28/38 GHz quad port MIMO antenna for 5G and beyond applications," *Scientific Reports*, Vol. 15, 44195, 2025.

[19] Tiwari, R. N., D. Sharma, P. Singh, B. G. Kullayappa, P. Kumar, B. R. Swamy, G. P. Kumar, and S. Rajasekaran, "Triple band lateral 4-port flexible MIMO antenna for millimeter wave applications at 24/28/38 GHz," *Results in Engineering*, Vol. 26, 104678, 2025.

[20] Gayathri, R., K. Kavitha, D. R. Kumar, and P. Sundaravadivel, "Miniaturized dual-band MIMO antenna with high gain and isolation for mm-Wave applications," *Scientific Reports*, Vol. 16, 7402, 2026.

[21] Nagendra, R., S. S. Vali, N. Divya, R. Surendra, *et al.*, "2×2 MIMO rectangular patch antenna array for 5G applications operating at 28/38 GHz," in *2025 2nd International Conference on Intelligent Algorithms for Computational Intelligence Systems (IACIS)*, 1–7, Hassan, India, 2025.

[22] Elabd, R. H. and A. J. A. Al-Gburi, "Low mutual coupling miniaturized dual-band quad-port MIMO antenna array using decoupling structure for 5G smartphones," *Discover Applied Sciences*, Vol. 6, No. 4, 189, 2024.

[23] Elabd, R. H. and A. J. A. Al-Gburi, "Super-compact 28/38 GHz 4-port MIMO antenna using metamaterial-inspired EBG structure with SAR analysis for 5G cellular devices," *Journal of Infrared, Millimeter, and Terahertz Waves*, Vol. 45, No. 1, 35–65, 2024.

[24] Elabd, R. H., R. E. A. Shehata, A. J. A. Al-Gburi, and M. E. Mousa, "Compact and high-performance MIMO antenna with metasurface integration for millimeter-wave and next-generation 6G applications," *Journal of Infrared, Millimeter, and Terahertz Waves*, Vol. 46, No. 9, 62, 2025.

[25] Gaber, S. M., R. A. Kareem, and A. A. Ibrahim, "High isolation quad ports MIMO antenna loaded with FSS for 5G communication," *Scientific Reports*, Vol. 15, No. 1, 20167, 2025.

[26] Haque, M. A., M. S. Ahammed, S. Socheatra, R. A. Ananta, M. J. H. Nirob, N. S. S. Singh, N. M. Jizat, S. Alsowail, and S. S. Al-Bawri, "Machine learning based compact MIMO antenna array for 38 GHz millimeter wave application with robust isolation and high efficiency performance," *Results in Engineering*, Vol. 25, 104006, 2025.

[27] Haque, M. A., R. A. Ananta, M. S. Ahammed, J. H. Nirob, N. S. S. Singh, L. C. Paul, R. I. Alkanhel, A. A. A. El-Latif, M. Almousa, and A. A. Ateya, "High-isolation dual-band MIMO antenna for next-generation 5G wireless networks at 28/38 GHz with machine learning-based gain prediction," *Scientific Reports*, Vol. 15, No. 1, 20782, 2025.

[28] Kiani, S. H., B. G. P. Shariff, D. A. Sehrai, M. Abdullah, T. Ali, A. D. Algarni, H. Elmannai, and I. M. Ibrahim, "High-performance four-element self-decoupled MIMO antenna system for n260 band applications," *Journal of Infrared, Millimeter, and Terahertz Waves*, Vol. 46, No. 9, 64, 2025.

[29] Kiani, S. H., B. G. P. Shariff, T. Ali, M. A. Khan, H. Elmannai, A. D. Algarni, M. I. Ibrahim, and M. Dalarsson, "Window-shaped mmwave MIMO antenna for 5G devices using characteristics mode analysis," *International Journal of Antennas and Propagation*, Vol. 2026, No. 1, 1928509, 2026.

[30] Mistri, R. K., A. K. Singh, S. K. Mahto, R. Sinha, A. J. A. Al-Gburi, M. M. Ismail, and K. Alhassoon, "An eight-element MIMO antenna system supporting dual bands for 5G mobile, FSS, and DBS communication," *Progress In Electromagnetics Research B*, Vol. 107, 125–137, 2024.

[31] Khan, M. K., S. Liu, and M. I. Khan, "A wideband eight-port MIMO antenna with reduced mutual coupling for future 5G mm-Wave applications," *Sensors*, Vol. 25, No. 2, 484, 2025.

[32] Kiani, S. H., M. I. Ibrahim, B. G. P. Shariff, M. A. Khan, A. A. Mugheri, T. Ali, U. Rafique, H. Mostafa, and M. Dalarsson, "Dual-key slot mmwave antenna array with dual-band performance at 28 GHz and 38 GHz using characteristic mode analysis," *Scientific Reports*, Vol. 16, No. 1, 3040, 2026.

[33] Kiani, S. H., U. Rafique, N. Shoaib, M. I. Abbasi, H. Elmannai, M. I. Ibrahim, and M. Dalarsson, "Low-profile metasurface-backed wideband antenna array for mm-Wave applications," *Scientific Reports*, Vol. 16, 8619, 2026.

[34] Rahman, M. A., S. S. Al-Bawri, S. S. Alharbi, W. M. Abdulkawi, N. M. Jizat, M. T. Islam, and A.-F. A. Sheta, "3D highly isolated 6-port tri-band MIMO antenna system with 360 coverage for 5G IoT applications based machine learning verification," *Scientific Reports*, Vol. 15, No. 1, 204, 2025.

[35] Jayanthi, K. and A. M. Kalpana, "Design of six element MIMO antenna with enhanced gain for 28/38 GHz mm-Wave 5G wireless application," *Computer Systems Science and Engineering*, Vol. 46, No. 2, 1689–1705, 2023.

[36] Shariff, B. G. P., T. Ali, P. Kumar, S. Pathan, G. D. G. Simha, P. R. Mane, M. G. N. Alsath, and A.-A. A. Boulogeorgos, "Dual-band compact six-element millimeter wave MIMO antenna: Design, characterization, and its application for V2V communication," *IEEE Access*, Vol. 12, 97 951–97 968, 2024.

[37] Ahmad, J. and M. Hashmi, "Reduced inter-element interference mmWave MIMO antenna and its application in WBAN," *IEEE Access*, Vol. 13, 70 947–70 963, 2025.